Frictiotaxis underlies adhesion-independent durotaxis

Adam Shellard[1*], Kai Weißenbruch[1*], Peter A. E. Hampshire[2,3], Namid R. Stillman[1],

Christina L. Dix[4], Richard Thorogate[5], Albane Imbert[4], Guillaume Charras[1,5], Ricard

Alert[2,3,6,**], Roberto Mayor[1,7,**].

[1]*Department of Cell and Developmental Biology, University College London, Gower Street,*

London, WC1E 6BT, UK

[2]*Max Planck Institute for the Physics of Complex Systems, Nöthnitzerst. 38, 01187, Dresden,*

Germany

[3]*Center for Systems Biology Dresden, Pfotenhauerst. 108, 01307, Dresden, Germany*

[4]*The Francis Crick Institute, 1 Midland Road, London, NW1 1AT, UK*

[5]*London Centre for Nanotechnology, University College London, London, WC1H 0AH, UK*

[6]*Cluster of Excellence Physics of Life, TU Dresden, 01062, Dresden, Germany*

[7]*Center for Integrative Biology, Faculty of Sciences, Universidad Mayor, Santiago, Chile*

* Co-first authors

** Corresponding authors: R.A. (Email: ralert@pks.mpg.de), R.M. (Email:

r.mayor@ucl.ac.uk)

20   Cells move directionally along gradients of substrate stiffness, a process called durotaxis. The

21   current consensus is that durotaxis relies on cell-substrate focal adhesions to sense stiffness

22   and transmit forces that drive directed motion. Therefore, focal adhesion-independent

23   durotaxis is thought to be impossible. Here, we show that confined cells can perform

24   durotaxis despite lacking strong or specific adhesions. This durotactic migration depends on

25   asymmetric myosin distribution and actomyosin retrograde flow. We show that the

26   mechanism of this adhesion-independent durotaxis is that stiffer substrates offer higher

27   friction. We propose a physical model that predicts that non-adherent cells polarise and

28   migrate towards regions of higher friction – a process that we call frictiotaxis. We

29   demonstrate frictiotaxis in experiments by showing that cells migrate up a friction gradient

30   even when stiffness is uniform. Our results broaden the potential of durotaxis to guide any

31   cell that contacts a substrate and reveal a new mode of directed migration based on friction,

32   with implications for immune and cancer cells, which commonly move with non-specific

33   interactions.

The ability of cells to migrate following environmental gradients underlies many aspects of development, homeostasis and disease[1,2]. Cells follow gradients in the stiffness of their substrate, a process called durotaxis that has been demonstrated in multiple cell types *in vitro* and *in vivo*[3-7]. The prevailing mechanistic view of durotaxis involves the cells' actomyosin machinery producing contractile forces that pull on the underlying substrate through focal adhesions. These pulling forces then bias cell motion in one direction, typically toward the stiffer substrate[5,8-10]. These physical models are supported by experimental evidence, and an essential component of all of them is strong cell-substrate adhesions. It is thus believed that cells lacking adhesions must be incapable of sensing stiffness gradients. Whether cells lacking cell-matrix adhesions can respond to mechanical gradients is widely acknowledged as a vital question[11-14] that has been unaddressed. Its importance is highlighted by the fact that adhesion-independent motility is a fundamental mode of migration, classically exhibited by various cancer and immune cells, but which can be triggered in practically any cell type by providing 3D confinement[15,16].

Microchannels with tuneable stiffness

Part of the challenge in addressing whether cells migrating without adhesions are capable of responding to stiffness gradients, or indeed the role of substrate stiffness in the context of 3D adhesion-independent motility in general, lies in the technical challenge of fabricating confined cellular environments of tuneable stiffness that are necessary to study adhesion-independent migration[12]. Adhesion-independent motility has commonly been studied using the 'under agarose assay' in which cells emigrate from a free region into confinement between agarose and glass. However, this method is unable to differentiate between the effect of confinement and the effect of compression since cells must deform their substrate to move. A newer method uses microchannels fabricated with polydimethylsiloxane (PDMS). However, this material exhibits stiffness in the MPa range, far from physiologically relevant

59   levels of most tissues, and offers little ability to tune rigidity. We developed a novel and easy-

60   to-use method in which mobile and deformable cells spontaneously migrate into and within

61   agarose-surrounded preformed microchannels (Fig. 1a). Fabricating microchannels with

62   agarose offers the potential to investigate cells within substrates of physiologically relevant

63   stiffnesses[17]. The dimensions of the channel are determined by a PDMS mould that provides

64   reliable confinement irrespective of microchannel dimensions (Fig. 1b,c and Extended Data

65   Fig. 1a-c) and is unaffected by the stiffness of the substrate (Fig. 1e,g and Extended Data Fig.

66   1d,e). The stiffness of the microchannel is tuned by the concentration of agarose (Fig. 1d).

67   Fluorospheres did not show directed motion within microchannels (Extended Data Fig. 1f,g),

68   confirming that pressure-driven fluid flow was not a factor in this setup. Importantly,

69   stiffness gradients can be created by combining solutions with different agarose

70   concentrations together during microchannel assembly (Fig. 1h,i).

71   To test our setup as a valid means of assaying confined non-adherent cellular motility, we

72   used a non-adherent subline of Walker 256 carcinosarcoma (henceforth Walker) cells as a

73   well-validated model of a cell type that moves without using specific substrate adhesions and

74   without focal adhesions[18,19]. Although Walker cells are able to attach to fibronectin, they are

75   completely non-adhesive on agarose or on glass coated with PLL-PEG (Fig. 2a,b, Extended

76   Data Fig. 2). Furthermore, Walker cells introduced into the agarose microchannel setup

77   exhibited classical amoeboid motion characterised by bleb-based rather than lamellipodium-

78   based motility (Fig. 2c,d and Supplementary Video 1), fast migration (Fig. 2e) and lack of

79   focal adhesions (Fig. 2f,g). Together, these observations indicate that Walker cells are non-

80   adhesive in our agarose microchannel setup.

81   **Adhesion-independent durotaxis**

82   To directly address whether cells are capable of undergoing durotaxis in an adhesion-

83   independent manner, agarose microchannels were fabricated to have either uniform stiffness

84   or a stiffness gradient (Fig. 3a). We tracked migratory cells that entered regions of the

85   microchannel which exhibited either uniform or graded stiffness. Cells entering substrate of

86   uniform stiffness had a moderate tendency to repolarise and move back, whereas cells

87   entering a stiffness gradient were characterised by much higher persistence as they migrated

88   toward the stiff substrate (Fig. 3b-e and Supplementary Video 2). In addition, cells exhibited

89   a higher migration speed at higher stiffness values (Fig. 3f and Extended Data Fig. 3). Like

90   Walker cells, HL60 neutrophil-like cells, a cell type with a well-described amoeboid

91   behaviour[20], also exhibited preferred motion toward stiffer substrate (Extended Data Fig. 4).

92   Together, these results reveal adhesion-independent durotaxis may be a generalisable

93   phenomenon.

Ameboid durotaxis depends on actomyosin flow

95   It has previously been described that amoeboid migration on substrates of uniform stiffness

96   depends on actomyosin retrograde flow[18]. We therefore asked whether actomyosin retrograde

97   flow was also observed in our cells undergoing adhesion-independent durotaxis. Walker cells

98   expressing myosin-GFP were placed in the agarose microchannels with either uniform

99   stiffness or a stiffness gradient, followed by time-lapse imaging. Cells exhibited an

100   accumulation of myosin at the rear and a clear myosin retrograde flow (Fig. 4a,b, Extended

101   Data Fig. 5a-c and Supplementary Video 4&5). Upon cell repolarisation, the direction of

102   retrograde actomyosin flow was reversed, leading to accumulation of actomyosin at the new

103   cell rear (Fig. 4b and Supplementary Video 4). A clear positive correlation between

104   actomyosin flow and cell speed was observed (Fig. 4c and Extended Data Fig 5c). To

105   determine whether myosin was required for adhesion-independent durotaxis, myosin activity

106   was reduced by treating cells with the ROCK inhibitor Y-27632. A clear loss in the rear

107   accumulation of myosin (Fig. 4d), retrograde flow (Extended Data Fig 5d), bleb formation

108   (Fig. 4g), and impairment of migration was observed in treated cells compared with control

109   cells (Fig. 4e,f,h and Supplementary Video 6). These observations show that rear

110   accumulation of myosin dependent on actomyosin retrograde flow is required for adhesion-

111   independent durotaxis.

An active gel model of amoeboid migration predicts frictiotaxis

113   Given that amoeboid cells lack focal adhesions, it was unclear how these cells were able to

114   durotax. We hypothesised that regions of higher stiffness may offer higher friction, which

115   arises from non-specific molecular interactions between the cell membrane and the channel

116   walls[18]. We also hypothesised that, in the absence of active forces pulling the substrate, this

117   passive friction would cause amoeboid cells to undergo durotaxis.

118   We investigated this hypothesis through a physical model of amoeboid motility which treats

119   the actomyosin network in the cell cortex as an active gel[13,15,16,18,21-25]. In this model, myosin-

120   generated contractility triggers an instability whereby the gel concentrates towards one side,

121   which becomes the cell rear (Fig. 5a). This concentration profile drives retrograde

122   actomyosin flow, which propels the cell forward. In the absence of external gradients,

123   symmetry is broken spontaneously. The cell can thus move either left or right (Fig. 5a),

124   consistent with our experimental observations of repolarisation events in uniform channels

125   (Fig. 3c,d).

126   To benchmark this model, defined by Eqs. S13-S16 in the Supplementary Note, we solved it

127   numerically and obtained the steady-state actomyosin concentration profile (Methods). This

128   profile fits the experimentally measured profile of myosin intensity (Extended Data Fig. 6-7,

129   Table I, see Methods), which shows that the model captures the myosin-driven amoeboid

130   migration in our experiments.

131   Within the framework of this model, we next asked what would happen if the cells were

132   exposed to an external friction gradient. We show that, in the model, a friction gradient can

133   break the symmetry and yield migration toward regions of higher friction. Starting from an

134   unpolarised state with uniform gel concentration, contractile stresses from the cell poles

135   generate faster cortex flows in low-friction areas. These flows concentrate the gel towards the

136   low-friction side, which thus becomes the cell rear (Fig. 5b).

137   To demonstrate this mechanism of symmetry breaking, we considered force balance for the

138   actomyosin gel:

139
$$\xi \phi v = \frac{d\sigma}{dx}. \tag{1}$$

140   The left-hand side represents gel-substrate friction, which is proportional to the coefficient

141    $\xi(x)$, the volume fraction $\phi(x)$ of the gel, and its velocity $v(x)$ with respect to the substrate.

142   The right-hand side represents the forces generated within the gel. These forces arise from

143   gradients of the gel stress $\sigma = \sigma_a + \sigma_v - \Pi$, which includes contributions from active

144   contractility, $\sigma_a = \zeta\phi$, gel viscosity $\sigma_v = \eta\phi \, dv/dx$, and osmotic pressure $\Pi =$

145    $\alpha(\phi - \phi_0)^3 - \gamma \, d^2\phi/dx^2$ [24]. Here, ζ, η, α, and γ are material parameters described in more

146   detail in Reference[24] and in the Supplementary Note, and ϕ_0 is the equilibrium volume

147   fraction of the gel.

148   Because the cell poles are not subject to substrate friction, they undergo the contractile

149   instability earlier and faster than the rest of the gel. The resulting pole contraction pulls in gel

150   from the central region of the cell (Fig. 5b). In the central region, the gel starts in the

151   unpolarised state with uniform gel concentration $\phi(x) = \phi_0$, for which the force balance Eq.

152   (1) reduces to

154
$$\xi v = \eta \frac{d^2 v}{dx^2}. \tag{2}$$

153

155   To capture the mechanism of symmetry breaking, we solve this force balance close to the two

156   ends of the central region, which are subject to a stress σ_{pole} arising from pole contraction

157   and have different friction coefficients ξ_- and ξ_+, with $\xi_- < \xi_+$. Thus, we obtain the

158   velocities of the two ends, v_+ and v_- (Supplementary Note):

$$v_\pm = \pm \frac{\sigma_{pole}}{\sqrt{\eta\, \xi_\pm}}. \tag{3}$$

160

159

161   As illustrated in Fig. 5b, this result shows that the gel flows faster towards the pole in the

162   low-friction region, which leads to gel accumulation towards that side and subsequent cell

163   migration towards high-friction regions.

164   Overall, our theory predicts a mode of cell migration guided by friction gradients (Fig. 5b),

165   which we call frictiotaxis. These results suggest that cells without strong focal adhesions

166   perform durotaxis by exploiting gradients in friction rather than stiffness variations.

167   **Substrate friction and stiffness are correlated**

168   To test this idea in experiments, we first probed the relationship between stiffness and friction

169   by performing lateral force microscopy (LFM) on the agarose microchannels across the

170   stiffness range in which we observed durotaxis. LFM measures the torsional deformation of

171   the micro-mechanical cantilever of an atomic force microscope during contact mode,

172   enabling the measurement of frictional properties. We found that, in accordance with our

173   hypothesis, stiffer substrates exhibited higher friction forces (Fig. 6a).

174   **Experimental evidence of frictiotaxis**

175   If amoeboid durotaxis is based on friction, it should be impaired if the channel walls are

176   passivated with polyethylene glycol (PEG), which has been shown to provide low-friction

177   substrates[18,26] (Fig. 6b). Additionally, cells should be capable of directed migration when

178   stiffness is uniform, but friction is graded.

179   To test the first prediction, we employed a previously described method in which agarose is

180   coupled to proteins after the surface is activated with cyanogen bromide, enabling functional

181   interactions between the cell and the coated surface[27,28]. As a proof of principle, cells adhered

182   strongly to fibronectin-coated agarose gels (Extended Data Fig. 8a). We thus coated agarose

183   microchannels exhibiting a stiffness gradient with PLL-g-PEG (Extended Data Fig. 8b,c).

184   Cells migrating through such channels had impaired durotaxis, compared to controls (Fig. 6c-

185   e). Thus, durotaxis is impaired by a reduced friction despite the presence of a stiffness

186   gradient.

187   To address whether gradients in friction are sufficient to guide cell migration in the absence

188   of adhesions, we generated gradients in friction by micropatterning gradients of bovine serum

189   albumin (BSA), which provides high friction, and PEG, which provides low friction[18], onto

190   glass and within PDMS microchannels (Fig. 6f,h and Extended Data Fig. 8d,e), such that

191   regions without BSA contained PEG. By performing LFM, we validated that BSA-coated

192   regions provided higher friction than PEG-coated regions (Fig. 6b), which supports previous

193   evidence[18]. We observed cells moving toward areas of higher friction when they migrated in

194   these channels, as opposed to randomly directed motion when friction was uniform (Fig. 6h-j

195   and Supplementary Video 7). Motion guided by friction gradients was previously

196   conceptualized[29] and demonstrated in magnetic colloidal particles[30]. Here, our experimental

197   data confirm that cells perform frictiotaxis, and they suggest that this mode of directed

198   migration provides the mechanism for adhesion-independent durotaxis.

Discussion

200   Altogether, our study contributes to the growing field questioning how the physical

201   environment modulates adhesion-independent migration[22,31,32]. Our results reveal that strong

202   and specific adhesions are redundant for durotaxis thanks to non-specific friction forces,

203 which enable preferential movement toward stiffer substrates because stiffness and friction

204 are correlated. In practice, different tissues may exhibit different stiffness-friction

205 relationships, thus affecting cell response. Although cells performing amoeboid migration

206 might have weak adhesions, the mechanism of directed motion that we reveal is entirely

207 based on friction. Accordingly, our model includes no adhesion, i.e., no resistance to normal

208 pulling forces, but just friction that opposes cell-substrate sliding.

209 Modulating only one physical variable, in this case stiffness, to investigate cell behaviour is a

210 major challenge. Despite establishing the dominant role of friction, we cannot rule out that

211 differential substrate deformation contributes to adhesion-independent durotaxis. In this

212 study, we used microchannels that were larger than the nucleus, because amoeboid cells use

213 the nucleus as a mechanical gauge in path-making decisions[33]. We also chose to use pre-

214 formed paths, rather than an 'under agarose assay', to rule out the role of compression on the

215 cells, since cells under compression must physically deform their surroundings to move,

216 which is more difficult when the substrate is stiffer[31]. Whether cell compression and other

217 physical inputs can act as guidance cues for adhesion-independent cell motility remains an

218 open question. Notably, however, geometric patterns can guide adhesion-independent

219 motility[22,34].

220 Finally, whether frictiotaxis and amoeboid durotaxis are physiologically relevant in the

221 complex *in vivo* environment, especially considering that chemotactic signals are extremely

222 potent drivers of directional cell migration, is also unknown. A promising candidate are

223 immune cells, which often need to traverse tissues of high density to reach target sites.

224 Adhesion-independent durotaxis could contribute significantly to this type of directed
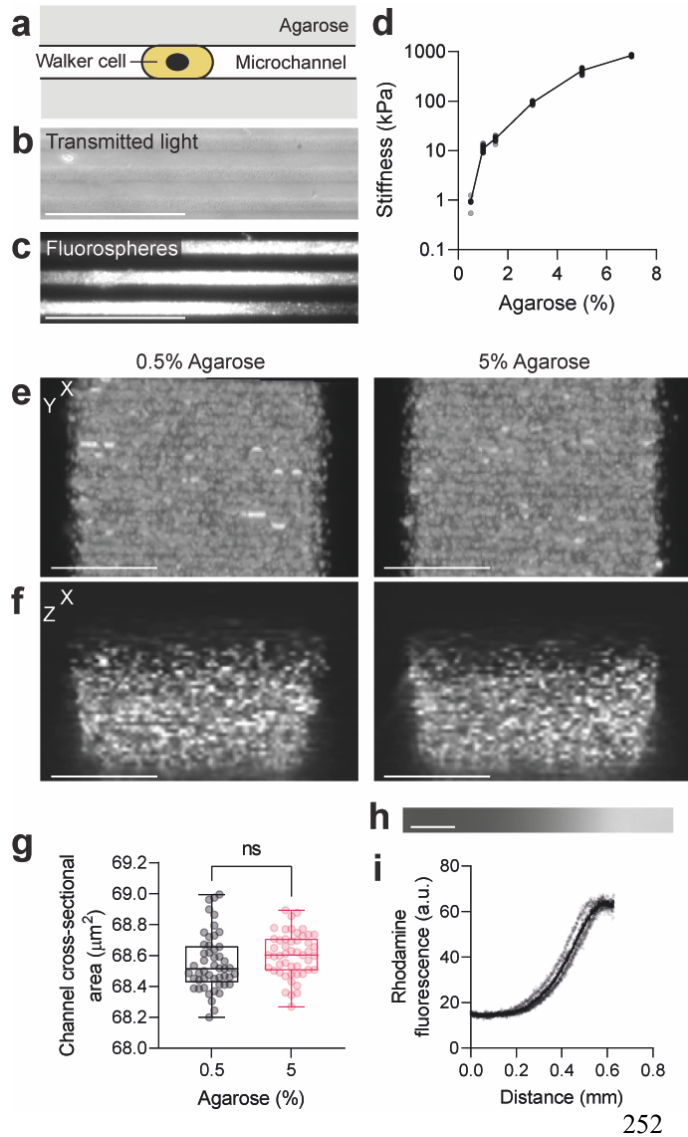
225 migration.

Figure 1. A microchannel system with tuneable stiffness and dimensions. a, Diagram of the microchannel assay. Microchannel dimensions determine the geometry of the setup and the agarose surrounding the cell determines substrate stiffness. **b-c**, Agarose channels (**b**) filled with 0.2 µm fluorospheres (**c**). Scale bar, 100 µm. **d**, Stiffness measurements (mean ± s.d.) by nanoindentation of gels of different agarose concentration. Grey dots represent individual data points, black dots represent mean. *n* = 25 cells. **e-g**, Agarose microchannels (**e-f**; 0.5%, left; 5%, right) filled with 0.2 µm fluorospheres and imaged from below (**e**, maximum projection) and side-on (**f**). Channel cross-sectional area quantified (**g**). Scale bar, 5 µm. For **g**, n = 49 channels; unpaired two-tailed t test; ns, *P*>0.05 (exact: *P*=0.2229). **h-i**, A stiffness gradient visualized by immersing rhodamine dextran dye into one of the agarose solutions prior to subsequent diffusion and solidification (**h**) and quantification of the dye fluorescence over the gradient axis (**i**). Scale bar, 100 µm. Grey dots represent individual data points, black dots represent mean. *n* = 5 gels.
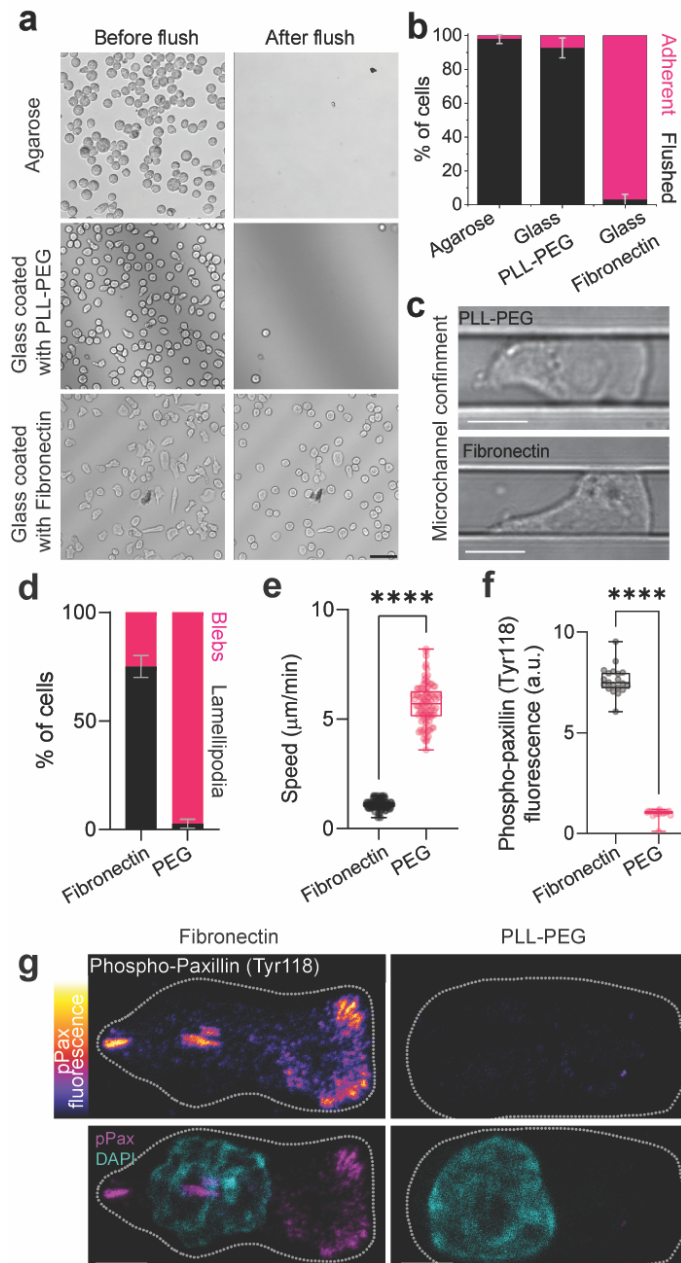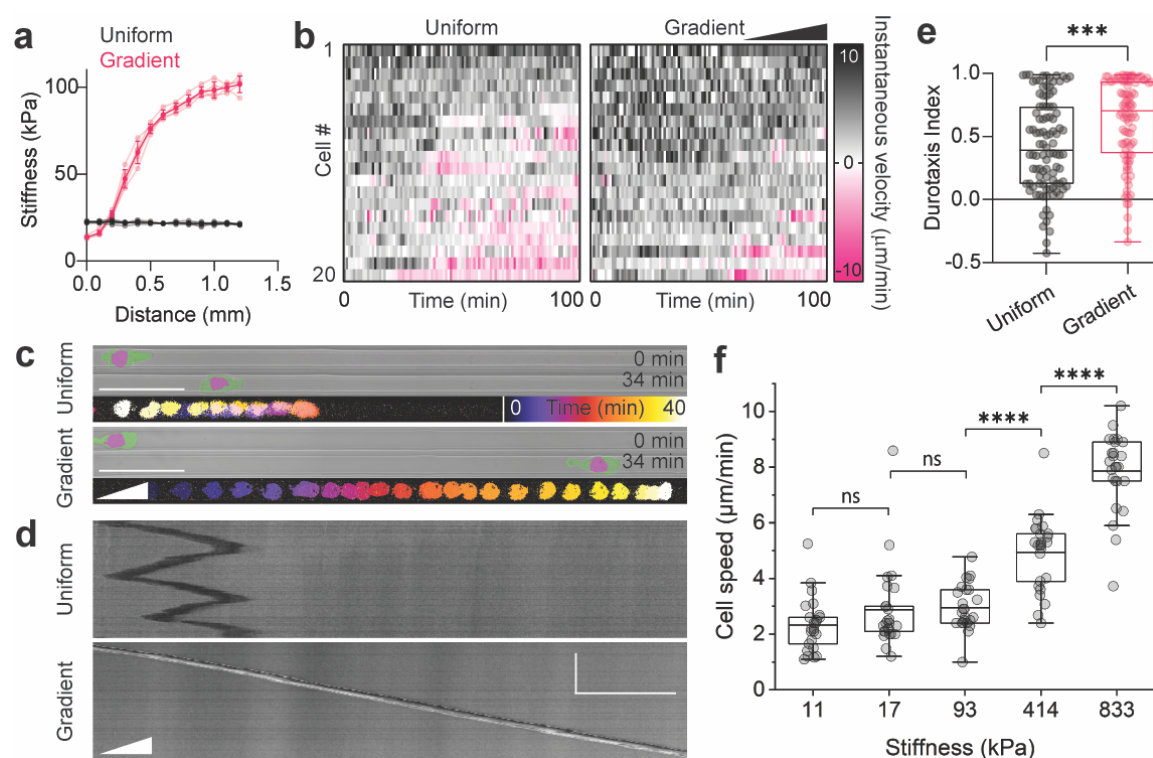
Figure 2. Walker cells exhibit adhesion-independent amoeboid migration in the microchannel system. a, Images of Walker cells on agarose, glass coated with PLL-PEG, and glass coated with fibronectin, before and after flushing the substrate with culture medium. Scale bar, 50 μm. **b**, Quantification of adherent and flushed fraction of cells after flushing the respective substrates. Bars represent mean ± s.d.; $N = 3$ experimental repeats. **c**, Example images of cells in non-adhesive (PLL-PEG, top) or adhesive (fibronectin, bottom) agarose microchannels. Scale bar, 10 μm. **d**, Quantification of lamellipodia and blebs by cells in adhesive (fibronectin) and non-adhesive (PEG) conditions. Bars represent mean ± s.d.; $N = 3$ experimental repeats. **e,** Speed of cells migrating within agarose microchannels with fibronectin or PEG coating. **f-g**, Immunostaining against phospho-paxillin (Tyr118) in Walker cells within agarose channels (**g**) and quantification (**f**) in which the underlying glass is coated with either PLL-PEG or fibronectin. Dotted white line represents the cell outline. Scale bar, 5 μm. $n = 100$ cells (**e, f**); two-tailed Mann-Whitney test; ****$P \leq 0.0001$.

Figure 3. Adhesion-independent durotaxis of Walker cells. a, Stiffness measurements (mean ± s.d.) from nanoindentation of uniform (black) and gradient (pink) microchannels. Opaque dots and lines represent mean; translucent dots and lines represent raw data. $n = 5$ gels each. **b**, Heat maps of the instantaneous velocity of representative cells migrating within microchannels of uniform or graded stiffness. $n = 20$ representative cells each. Each row represents a different cell. The *x*-axis represents time, with each box representing 1 min for a total of 100 min. Each heat map is ordered such that cells migrating forward (black) are at the top, and cells migrating backwards (pink) are at the bottom. **c**, Example pictures of cells at an earlier (top panels) and later (middle panels) time point, and temporal colour-coded projected tracks (bottom panels). Cells are tracked by a nuclear marker and membrane is pseudocoloured. Scale bar, 50 μm. **d**, Kymographs of the cells shown in (**c**). Scale bar, 50 μm (horizontal), 50 min (vertical). **e**, Quantification of durotaxis. $n = 100$ cells; two-tailed Mann-Whitney test; ***$P \leq 0.001$ (exact: $P = 0.0003$). **f**, Quantification of migration speed in microchannels of different stiffness regimes. $n = 25$ cells for each stiffness regime; two-tailed Mann-Whitney test; ns, $P > 0.05$ (11 versus 17: $P = 0.23258$; 17 versus 93: $P = 0.09795$), ****$P \leq 0.0001$.
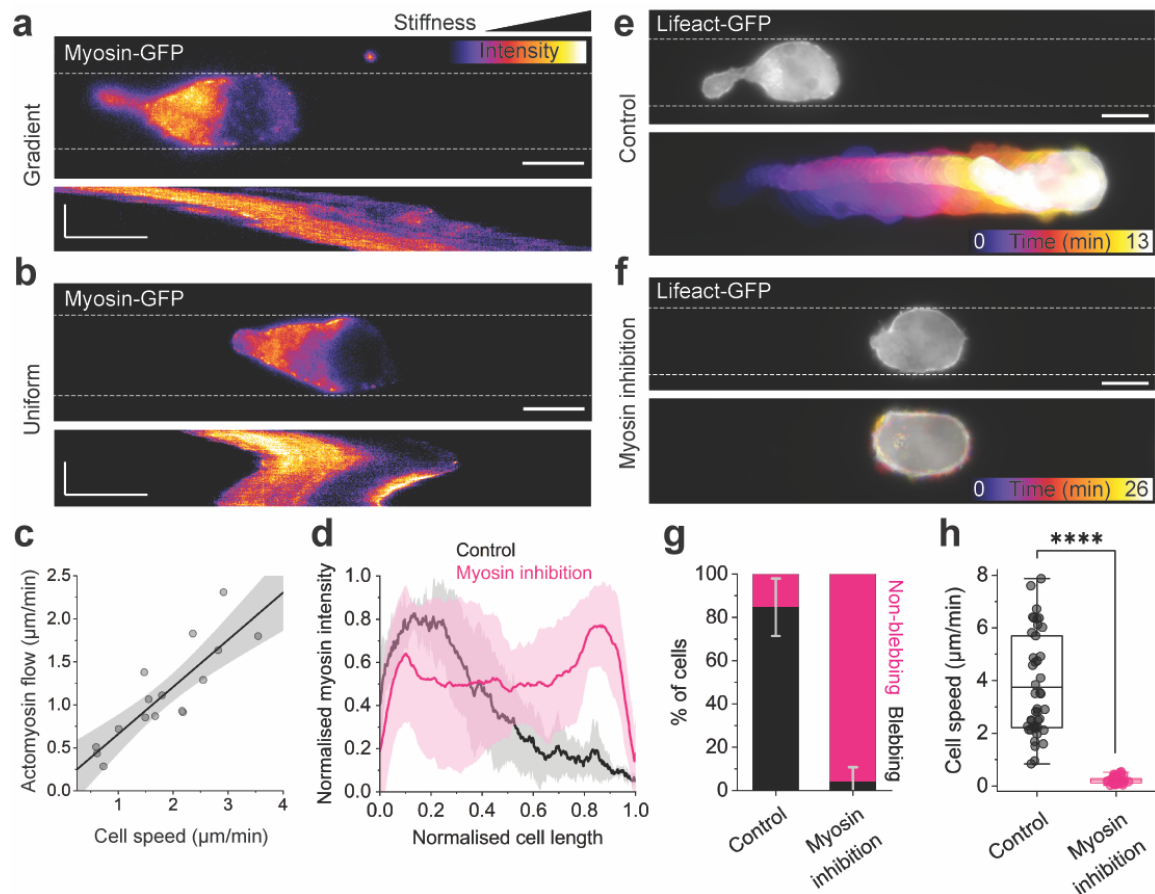
13
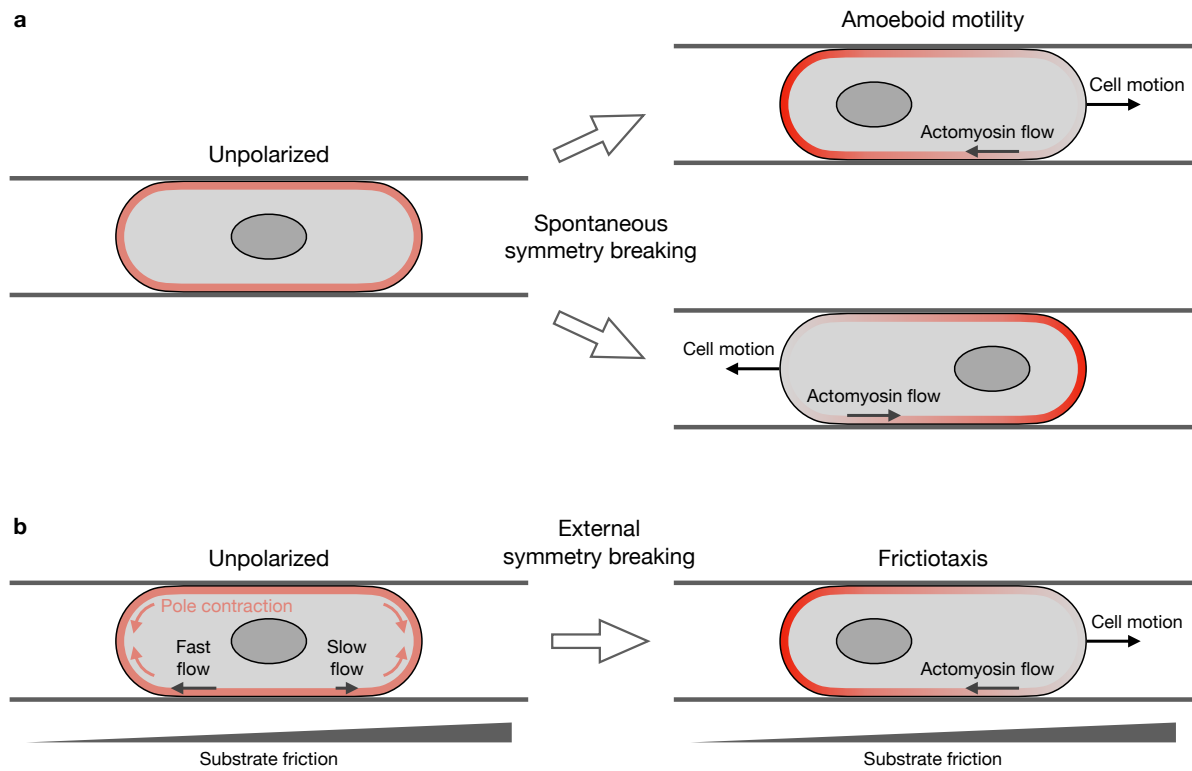
Figure 4. Adhesion-independent durotaxis depends on retrograde actomyosin flow. a-b, Still images and corresponding kymographs from timelapse records of Myosin-GPF-expressing Walker cells, migrating in microchannels with stiffness gradient (**a**) or uniform stiffness (**b**). Fluorescence signal was colour-coded, dotted lines represent channel boundaries. Scale bars, 10 µm in still images, 5 µm (horizontal) and 10 min (vertical) in kymographs. **c**, Correlation of actomyosin flow and migration speed. Coefficient of determination (R^2) = 0.73068. Grey areas depict upper and lower 95% confidence limits. Dots represent mean values of individual cells migrating over 400 s. Data points of $n = 8$ cells in stiffness gradients or uniform stiffness were picked randomly from $N = 3$ independent experiments each and pooled. **d**, Intensity profiles of Myosin-GFP signals along the front-rear axis of Walker cells in the absence (DMSO control, black line) or presence of 30 µM Y-27632 (Myosin inhibition, purple line). Myosin-GFP intensity and cell length were normalised for comparison. Solid lines plus transparent areas depict mean ± s.d. of $n = 6$ cells each, from $N=3$ independent experiments. **e-f**, Still images and corresponding colour-coded timelapse records of Lifeact-GPF-expressing Walker cells in microchannels of uniform stiffness; in the absence (**e**) or presence of 30µM Y-27632 (**f**). Dotted lines represent channel boundaries. Scale bars, 10 µm. **g**, Quantification of blebbing and non-blebbing fractions of cells under control (DMSO) or myosin inhibiting (30 µM Y-27632) conditions. Bars represent mean ± s.d. from $N = 3$ independent experiments. **h**, Quantification of migration speed in microchannels of uniform stiffness. $n = 43$ cells for control (DMSO) and $n = 47$ cells for myosin inhibition (30 µM Y-27632); two-tailed Mann-Whitney test; ****$P \leq 0.0001$.

14

a

Unpolarized

Amoeboid motility

Spontaneous symmetry breaking

Cell motion

Actomyosin flow

Cell motion

Actomyosin flow

b

Unpolarized

External symmetry breaking

Frictiotaxis

Pole contraction

Fast flow

Slow flow

Substrate friction

Cell motion

Actomyosin flow

Substrate friction

Figure 5. Model of frictiotaxis. a, In the absence of external gradients, unpolarised cells break symmetry spontaneously and display amoeboid motility either left or right. **b**, On a friction gradient, contractile stresses from the poles produce faster cortical flows on the lower-friction side. These flows break the symmetry and accumulate actomyosin towards the low-friction side, which drives frictiotaxis, that is directed cell migration towards higher friction.
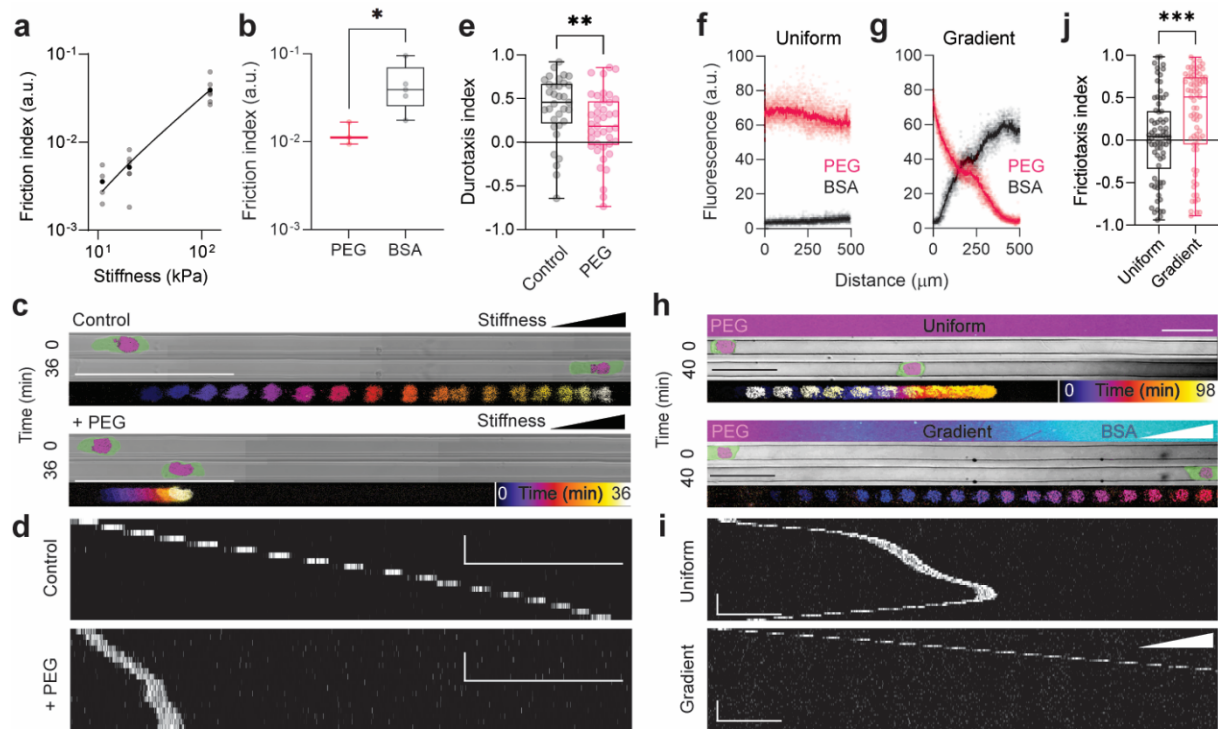
15

Figure 6. Friction-driven directed migration. a, Friction index versus stiffness in the gels; $n = 4$ (*in vitro*, at 11 kPa); $n = 6$ (*in vitro*, other stiffness values). **b**, Friction of PEG- or BSA-treated glass; $n = 3$ (PEG); $n = 5$ (BSA); two-tailed Mann-Whitney test; *$P \leq 0.05$ (exact: $P = 0.0357$). **c**, Pictures of Walker cells with a nuclear label and pseudocoloured membrane after t=0 min and t=36 min in stiffness-gradient microchannels without (Control, upper panel) or with PLL-PEG coating (+ PEG, lower panel). Temporal colour-coded projected tracks of the nucleus are shown in the bottom of each of the panels. Scale bars, 100 μm. **d**, Kymographs corresponding to the cells shown in **c**. Scale bars, 100 μm (horizontal) and 10 min (vertical). **e**, Durotaxis quantification; $n = 33$ cells; two-tailed Mann-Whitney test; **$P \leq 0.01$ (exact: $P = 0.0097$). **f-g**, Quantification of micropatterned PEG and BSA in microchannels with uniform and graded friction; $n = 10$ (PEG); $n = 9$ (BSA). Pale dots represent raw data; dark dots represent mean. **h**, Images of PLL-g-PEG/FITC and BSA-Alexa647 micropatterning (top panels), images of cells with a nuclear marker and pseudocoloured membrane at t=0 min and t=40 min (middle panels), and temporal colour-coded projected tracks (bottom panels). Scale bars, 50 μm. **i**, Kymographs corresponding to the cells shown in **h**. Cells were tracked via the nuclear marker. Scale bars, 50 μm (horizontal) and 10 min (vertical). **j**, Quantification of frictiotaxis index from $n = 74$ cells each; two-tailed Mann-Whitney test; ***$P \leq 0.001$ (exact: $P = 0.0010$).

16
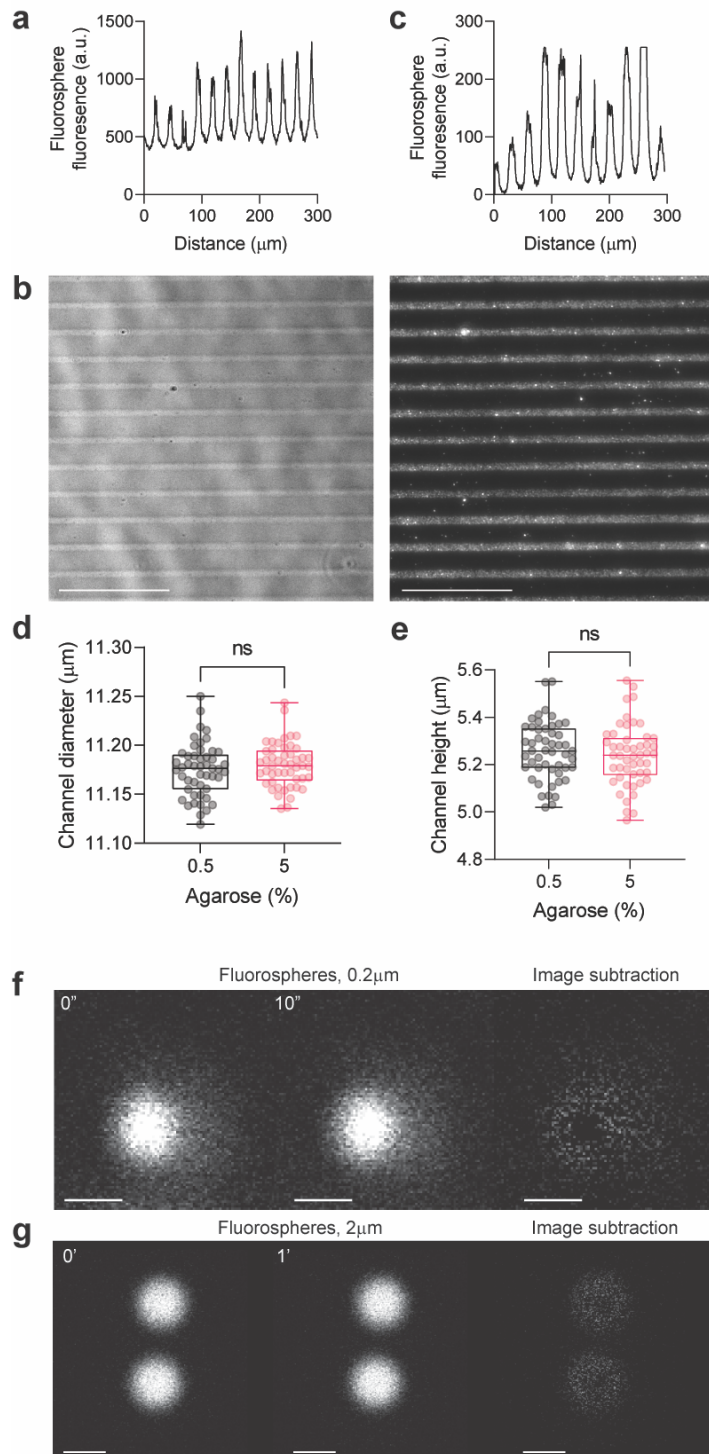
Extended Data Fig 1. The agarose microchannel assay. a-c, 5 µm agarose channels filled with 0.2 µm fluorospheres (**b**) and quantification along the orthogonal axis of fluorosphere-filled 10 µm (**c**) and 5 µm channels (**a**), as in Fig. 1c and Extended Data Fig. 1b, respectively. Scale bar, 100 µm. **d-e**, Channel dimensions quantified. Translucent dots represent individual data points. $N = 50$ channels; unpaired two-tailed t test; ns, $P > 0.05$ (exact: $P=0.3482$ in **d**; $P=0.4649$ in **e**). **f-g**, 0.2 µm (**f**) or 2 µm fluorospheres (**g**) in 10 µm agarose microchannels at different time points. The right panel is an image subtraction between the images. Scale bar, 0.5 µm (**f**); 2 µm (**g**).
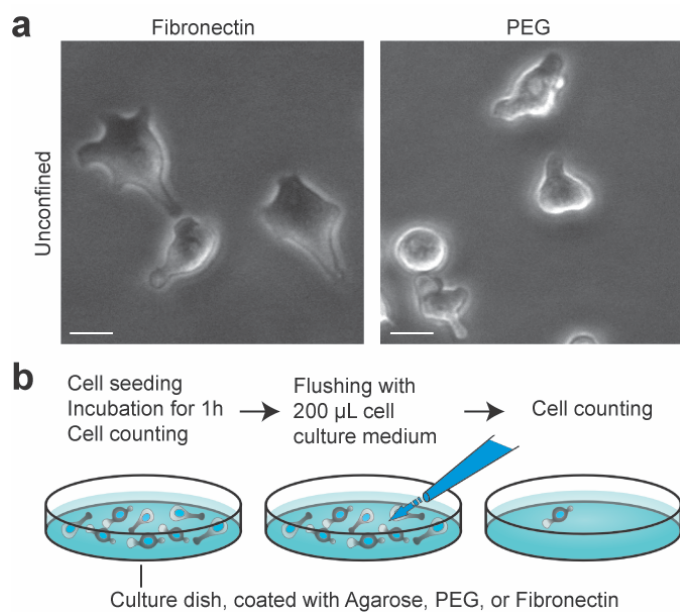
Extended Data Fig 2. Walker cells lack strong and specific adhesions. a, Pictures of cells in adhesive (fibronectin, left) or non-adhesive (PEG, right) conditions. Scale bar, 10 μm. **b**, Illustration depicting the principle and quantification of the flushing experiment.
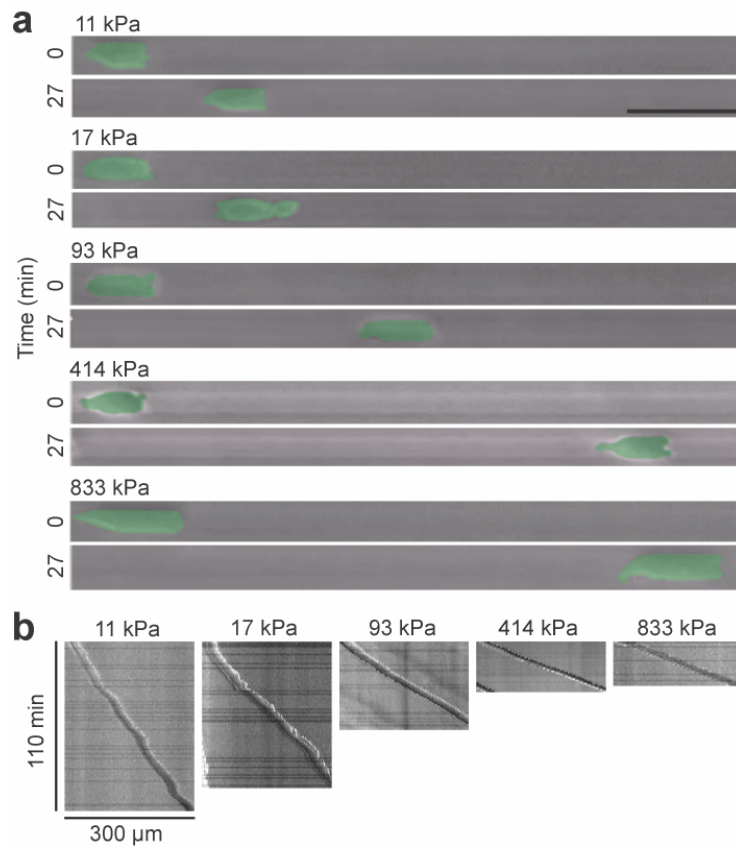
Extended Data Fig 3. Stiffness-dependent migration speed in microchannels. a, Pictures of cells with pseudocoloured membrane at early (t=0 min) and later (t=27 min) time points in microchannels of different stiffness regimes. Scale bar, 50 μm. **b,** Kymographs corresponding to the cells depicted in (**a**). Scale bars equal 300 μm (horizontal) and 110 min (vertical).

19
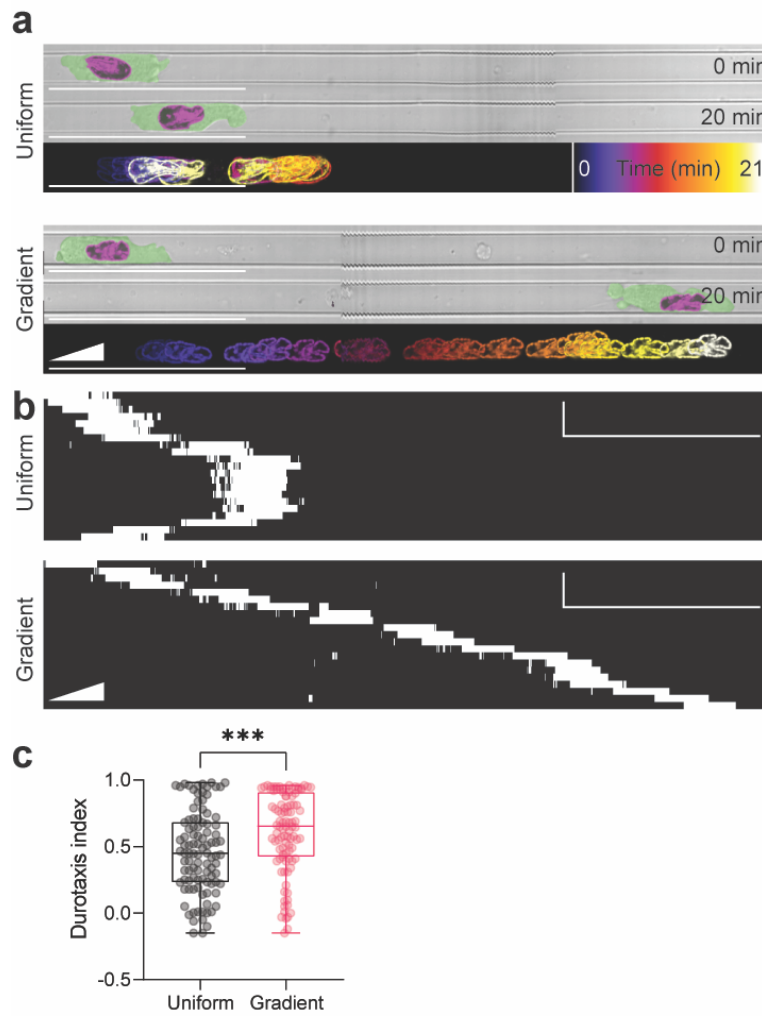
Extended Data Fig 4. Durotaxis of HL60 cells. a-b, Example cells at early and later time points (upper and middle panels, **a**), temporal colour-coded projections (bottom panels, **a**) and kymographs (**b**) in uniform and graded stiffness substrate. Cells were tracked by labelling the nucleus with Hoechst 33342 and the cell membrane was pseudocoloured. Images are stitched as described in the Methods. Scale bar, 50 μm. Vertical scale bar (**b**), 5 min. **c,** Durotaxis quantification. $n = 100$ cells; two-tailed Mann-Whitney test; ***$P \leq 0.001$ (exact: $P = 0.0006$).
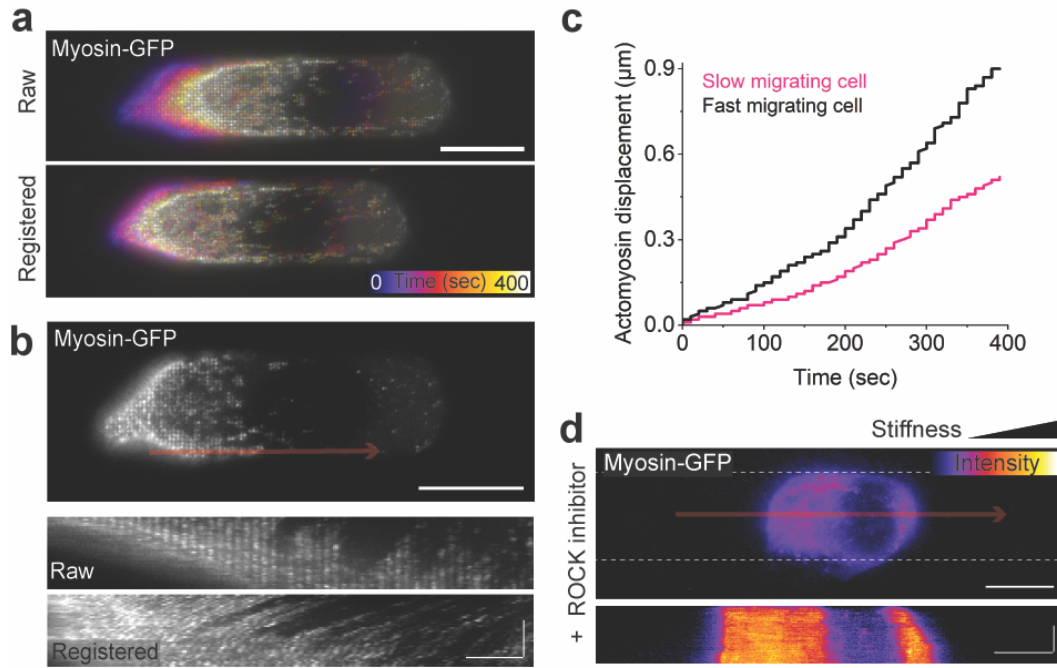
Extended Data Fig 5. Visualisation of retrograde actomyosin flow. a, Temporal colour-coded projection of a Myosin-GFP-expressing Walker cell before (raw_top panel) and after image registration (registered_bottom panel). Scale bar equals 10 µm. **b**, Kymographs of actomyosin flow, corresponding to the area along the red arrow in the upper panel, before (raw) and after image registration (registered). Scale bars, 10 µm in the upper panel; 5 µm (horizontal) and 200 s (vertical) in kymographs of lower panels. **c**, Examples of actomyosin displacement over time of a slow (1.47 µm/min) versus faster (2.16 µm/min) migrating cell in a microchannel with stiffness gradient. **d**, Colour-coded still image (upper panel) and Kymograph (lower panel, corresponding to the red arrow in the upper panel) of a Walker cell expressing Myosin-GFP, in a microchannel with stiffness gradient, and treated with 30 µM ROCK inhibitor (Y-27632). Dotted lines in the upper panel represent channel boundaries. Scale bars, 10 µm in upper panel; 10 µm (horizontal) and 20 min (vertical) in lower panel.
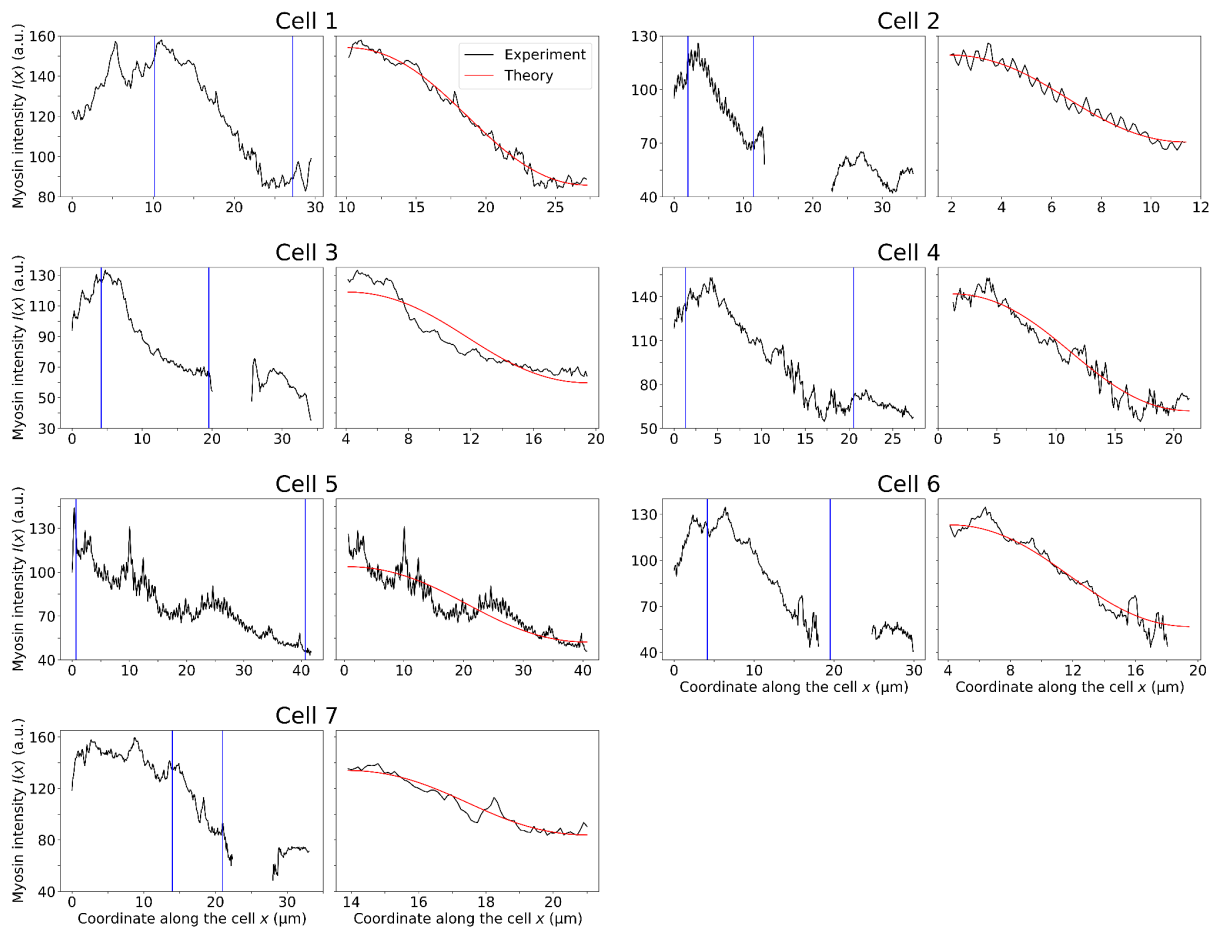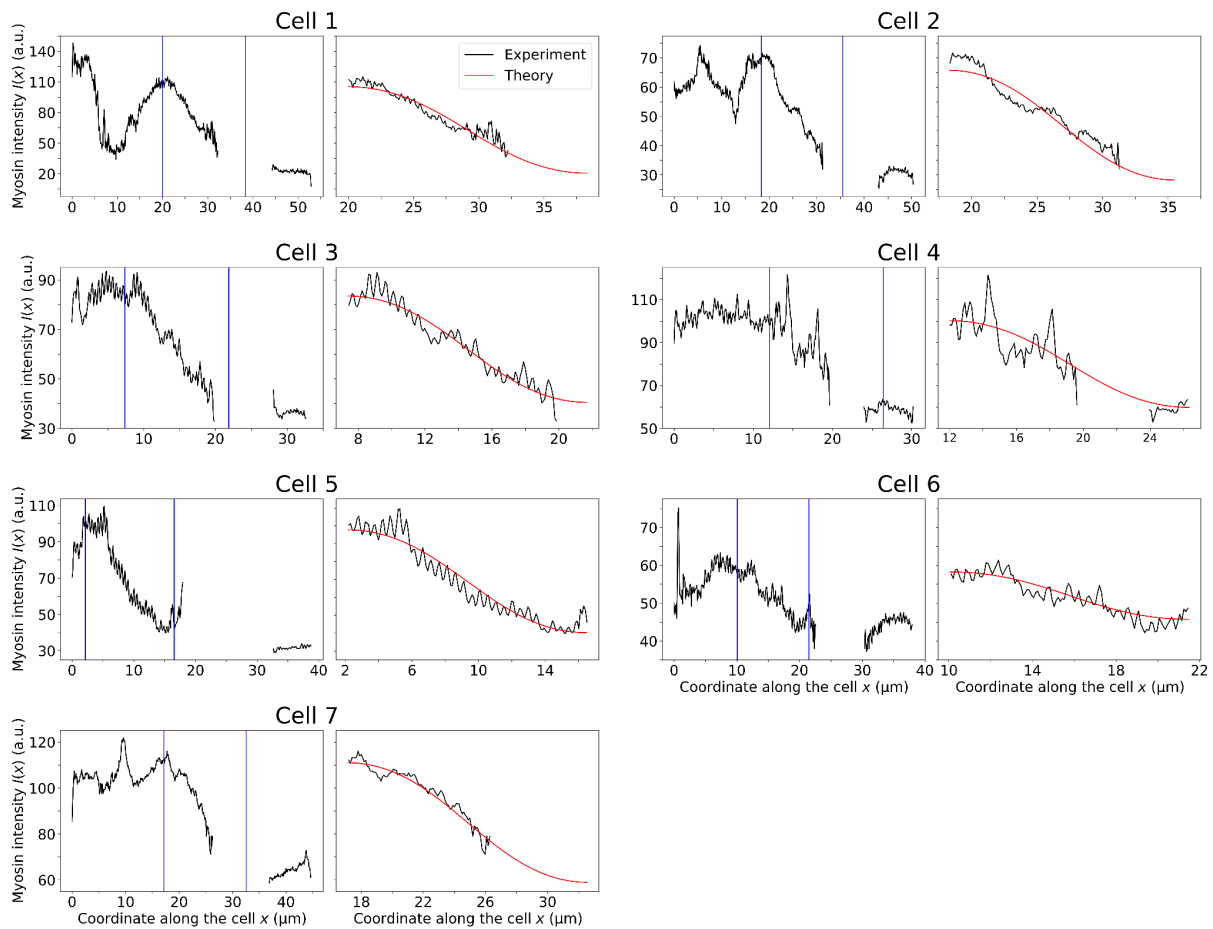
Extended Data Fig 6. Fits of the myosin intensity profiles for cells migrating on uniform friction. For each cell, the left column shows the myosin intensity profile along the cell at a single time frame. For some cells, there is missing intensity data at certain positions due to the nucleus displacing myosin. Only the data between the vertical blue lines is used for comparison to the steady-state solutions of the model. For each cell, the right column shows the fit of the steady-state solutions of the model (red) to the experimental data (black) selected from the left panels. Error bars are not visible as the errors of the mean of the experimentally measured intensities are typically around 1-5 a.u., which is much less than their absolute values. The fit parameter values are listed in Table I.
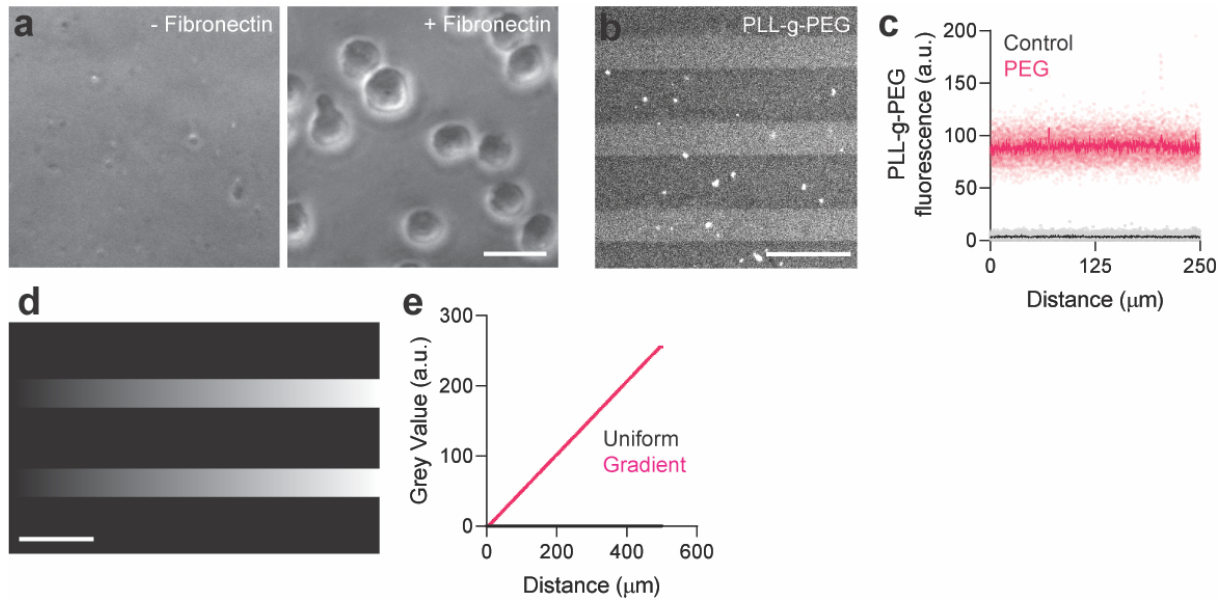
Extended Data Fig 7. Fits of the myosin intensity profiles for cells migrating on a friction gradient. For each cell, the left column shows the myosin intensity profile along the cell at a single time frame. For some cells, there is missing intensity data at certain positions due to the nucleus displacing myosin. Only the data between the vertical blue lines is used for comparison to the steady-state solutions of the model. For each cell, the right column shows the fit of the steady-state solutions of the model (red) to the experimental data (black) selected from the left panels. Error bars are not visible as the errors of the mean of the experimentally measured intensities are typically around 1-5 a.u., which is much less than their absolute values. The fit parameter values are listed in Table I.

448

Extended Data Fig. 8 Agarose activation, PEG coating and photopatterning gradients for frictiotaxis experiments. a, Cells adhere to a fibronectin-coated agarose gel. Medium was aspirated and flushed several times to remove any cells in suspension. Scale bar, 20 µm. **b-c**, PLL-g-PEG/FITC-coated or uncoated (control) agarose microchannels (**b**) and quantification of fluorescence (**c**); $n = 10$; pale colours represent raw data; dark colours represent mean. Scale bar, 20 µm. **d**, The designed photopattern which exhibits alternating control and gradient masks. Scale bar, 100 µm. **e**, Quantification of (**d**).

Cell #	Uniform friction		Friction gradient	
	$I_0/10$	$\bar{\alpha}/10^2$	$I_0/10$	$\bar{\alpha}/10^2$
1	12.0 ± 0.5	2.6 ± 0.5	6.3 ± 0.2	0.5 ± 0.2
2	9.5 ± 0.4	3.3 ± 0.8	4.7 ± 0.2	1.3 ± 0.7
3	8.9 ± 0.4	2.0 ± 1.0	6.2 ± 0.3	1.8 ± 0.7
4	10.1 ± 0.5	1.4 ± 0.6	8.0 ± 0.7	3.0 ± 3.0
5	7.8 ± 0.4	2.0 ± 2.0	6.9 ± 0.4	1.2 ± 0.6
6	9.0 ± 0.5	2.0 ± 1.0	5.2 ± 0.1	14.0 ± 1.0
7	10.9 ± 0.4	4.0 ± 2.0	8.5 ± 0.3	2.2 ± 0.5

Table I. Fit parameter values. Values of the scaling factor I_0 and the pressure coefficient $\bar{\alpha}$ obtained from the fits shown in Extended Data Figs. 6-7, which correspond to 7 cells migrating on uniform friction and 7 cells migrating on a friction gradient, respectively.

460   **Supplementary Video 1. Agarose microchannel assay.**

461   Walker cells migrating within 10 µm width microchannels within a 1% agarose substrate.

462   Movie length, 481 min. Scale bar, 100 µm.

463

464   **Supplementary Video 2. Adhesion-independent durotaxis.**

465   Walker cells undergo durotaxis without strong or specific adhesions to the substrate. Movie

466   length, 40 min. Scale bar, 50 µm.

467

468   **Supplementary Video 3. Stiffness-dependent migration speed.**

469   Migration speed of Walker cells increases with higher substrate stiffness. Movie length, 110

470   min.

471

472   **Supplementary Video 4. Myosin rear accumulation in gradient and uniform stiffness.**

473   In stiffness gradient and uniform stiffness microchannels, Myosin-GFP accumulates at the

474   cell rear and accumulation switches to the opposite pole when cells repolarise.

475

476   **Supplementary Video 5. Retrograde Myosin-GFP flow in raw and registered sequences.**

477   Retrograde Myosin-GFP flow is observed in raw and registered timelapse sequences.

478

479   **Supplementary Video 6. Myosin inhibition abrogates migration in microchannels.**

480   Upper panel: DMSO control. Lower panel: 30 µM Y-27632. Note that both cells in the lower

481   panel do not form blebs and do not migrate.

482

483   **Supplementary Video 7. Frictiotaxis.**

484   Walker cells undergo frictiotaxis on PEG-BSA gradients. Movie length, 98 min. Scale bar, 50

485   µm.

References

1   Shellard, A. & Mayor, R. All Roads Lead to Directional Cell Migration. *Trends Cell Biol* **30**, 852-868 (2020). https://doi.org:10.1016/j.tcb.2020.08.002

2   SenGupta, S., Parent, C. A. & Bear, J. E. The principles of directed cell migration. *Nat Rev Mol Cell Biol* **22**, 529-547 (2021). https://doi.org:10.1038/s41580-021-00366-6

3   Shellard, A. & Mayor, R. Collective durotaxis along a self-generated stiffness gradient in vivo. *Nature* **600**, 690-694 (2021). https://doi.org:10.1038/s41586-021-04210-x

4   Shellard, A. & Mayor, R. Durotaxis: The Hard Path from In Vitro to In Vivo. *Dev Cell* **56**, 227-239 (2021). https://doi.org:10.1016/j.devcel.2020.11.019

5   Sunyer, R. *et al.* Collective cell durotaxis emerges from long-range intercellular force transmission. *Science* **353**, 1157-1161 (2016). https://doi.org:10.1126/science.aaf7119

6   Lo, C. M., Wang, H. B., Dembo, M. & Wang, Y. L. Cell movement is guided by the rigidity of the substrate. *Biophys J* **79**, 144-152 (2000). https://doi.org:10.1016/S0006-3495(00)76279-5

7   Koser, D. E. *et al.* Mechanosensing is critical for axon growth in the developing brain. *Nat Neurosci* **19**, 1592-1598 (2016). https://doi.org:10.1038/nn.4394

8   Pallarès, M. E. *et al.* Stiffness-dependent active wetting enables optimal collective cell durotaxis. *Nature Physics* **19**, 279-289 (2023). https://doi.org:10.1038/s41567-022-01835-1

9   Alert, R. & Casademunt, J. Role of Substrate Stiffness in Tissue Spreading: Wetting Transition and Tissue Durotaxis. *Langmuir* **35**, 7571-7577 (2019). https://doi.org:10.1021/acs.langmuir.8b02037

10   Isomursu, A. *et al.* Directed cell migration towards softer environments. *Nat Mater* **21**, 1081-1090 (2022). https://doi.org:10.1038/s41563-022-01294-2

11   Yamada, K. M. & Sixt, M. Mechanisms of 3D cell migration. *Nat Rev Mol Cell Biol* **20**, 738-752 (2019). https://doi.org:10.1038/s41580-019-0172-9

12   Bodor, D. L., Ponisch, W., Endres, R. G. & Paluch, E. K. Of Cell Shapes and Motion: The Physical Basis of Animal Cell Migration. *Dev Cell* **52**, 550-562 (2020). https://doi.org:10.1016/j.devcel.2020.02.013

13   Paluch, E. K., Aspalter, I. M. & Sixt, M. Focal Adhesion-Independent Cell Migration. *Annu Rev Cell Dev Biol* **32**, 469-490 (2016). https://doi.org:10.1146/annurev-cellbio-111315-125341

14   Moreau, H. D., Piel, M., Voituriez, R. & Lennon-Duménil, A.-M. Integrating Physical and Molecular Insights on Immune Cell Migration. *Trends in Immunology* **39**, 632-643 (2018). https://doi.org:https://doi.org/10.1016/j.it.2018.04.007

15   Liu, Y.-J. *et al.* Confinement and Low Adhesion Induce Fast Amoeboid Migration of Slow Mesenchymal Cells. *Cell* **160**, 659-672 (2015). https://doi.org:https://doi.org/10.1016/j.cell.2015.01.007

16   Ruprecht, V. *et al.* Cortical contractility triggers a stochastic switch to fast amoeboid cell motility. *Cell* **160**, 673-685 (2015). https://doi.org:10.1016/j.cell.2015.01.008

17   Guimarães, C. F., Gasperini, L., Marques, A. P. & Reis, R. L. The stiffness of living tissues and its implications for tissue engineering. *Nature Reviews Materials* **5**, 351-370 (2020). https://doi.org:10.1038/s41578-019-0169-1

18   Bergert, M. *et al.* Force transmission during adhesion-independent migration. *Nat Cell Biol* **17**, 524-529 (2015). https://doi.org:10.1038/ncb3134

19   Bergert, M., Chandradoss, S. D., Desai, R. A. & Paluch, E. Cell mechanics control rapid transitions between blebs and lamellipodia during migration. *Proc Natl Acad Sci U S A* **109**, 14434-14439 (2012). https://doi.org:10.1073/pnas.1207968109

536 20 Wilson, K. *et al.* Mechanisms of leading edge protrusion in interstitial migration. *Nat*
537 *Commun* **4**, 2896 (2013). https://doi.org:10.1038/ncomms3896
538 21 Callan-Jones, A. Self-organization in amoeboid motility. *Front Cell Dev Biol* **10**,
539 1000071 (2022). https://doi.org:10.3389/fcell.2022.1000071
540 22 Reversat, A. *et al.* Cellular locomotion using environmental topography. *Nature* **582**,
541 582-585 (2020). https://doi.org:10.1038/s41586-020-2283-z
542 23 Callan-Jones, A. C. & Voituriez, R. Actin flows in cell migration: from locomotion
543 and polarity to trajectories. *Curr Opin Cell Biol* **38**, 12-17 (2016).
544 https://doi.org:10.1016/j.ceb.2016.01.003
545 24 Callan-Jones, A. C. & Voituriez, R. Active gel model of amoeboid cell motility. *New*
546 *Journal of Physics* **15**, 025022 (2013). https://doi.org:10.1088/1367-
547 2630/15/2/025022
548 25 Hawkins, R. J. *et al.* Spontaneous contractility-mediated cortical flow generates cell
549 migration in three-dimensional environments. *Biophys J* **101**, 1041-1045 (2011).
550 https://doi.org:10.1016/j.bpj.2011.07.038
551 26 Byun, S. *et al.* Characterizing deformability and surface friction of cancer cells. *Proc*
552 *Natl Acad Sci U S A* **110**, 7580-7585 (2013).
553 https://doi.org:10.1073/pnas.1218806110
554 27 Carlsson, J., Gabel, D., Larsson, E., Ponten, J. & Westermark, B. Protein-coated
555 agarose surfaces for attachment of cells. *In Vitro* **15**, 844-850 (1979).
556 https://doi.org:10.1007/BF02618038
557 28 Porath, J., Axen, R. & Ernback, S. Chemical coupling of proteins to agarose. *Nature*
558 **215**, 1491-1492 (1967). https://doi.org:10.1038/2151491a0
559 29 Carlsson, A. E. Mechanisms of Cell Propulsion by Active Stresses. *New J Phys* **13**
560 (2011). https://doi.org:10.1088/1367-2630/13/7/073009
561 30 Steimel, J. P., Aragones, J. L. & Alexander-Katz, A. Artificial tribotactic microscopic
562 walkers: walking based on friction gradients. *Phys Rev Lett* **113**, 178101 (2014).
563 https://doi.org:10.1103/PhysRevLett.113.178101
564 31 Gaertner, F. *et al.* WASp triggers mechanosensitive actin patches to facilitate immune
565 cell migration in dense tissues. *Dev Cell* **57**, 47-62 e49 (2022).
566 https://doi.org:10.1016/j.devcel.2021.11.024
567 32 Brunetti, R. M. *et al.* WASP integrates substrate topology and cell polarity to guide
568 neutrophil migration. *J Cell Biol* **221** (2022). https://doi.org:10.1083/jcb.202104046
569 33 Renkawitz, J. *et al.* Nuclear positioning facilitates amoeboid migration along the path
570 of least resistance. *Nature* **568**, 546-550 (2019). https://doi.org:10.1038/s41586-019-
571 1087-5
572 34 Le Berre, M. *et al.* Geometric friction directs cell migration. *Phys Rev Lett* **111**,
573 198101 (2013). https://doi.org:10.1103/PhysRevLett.111.198101
574 35 Ding, Y., Xu, G. K. & Wang, G. F. On the determination of elastic moduli of cells by
575 AFM based indentation. *Sci Rep* **7**, 45575 (2017). https://doi.org:10.1038/srep45575
576 36 Schiesser, W. E. & Griffiths, G. W. *A Compendium of Partial Differential Equation*
577 *Models: Method of Lines Analysis with Matlab.* (Cambridge University Press, 2009).
578 37 Schiesser, W. E. *The Numerical Method of Lines: Integration of Partial Differential*
579 *Equations.* (Elsevier Science, 2012).
580 38 Hamdi, S., Schiesser, W. & Griffiths, G. Method of lines. *Scholarpedia* **2**, 2859
581 (2007). https://doi.org:10.4249/scholarpedia.2859
582

Materials and Methods

Cell culture

Walker 256 carcinosarcoma cells (RRID:CVCL_4984), Walker myosin light chain-GFP

cells, and Walker Lifeact-GFP cells were a gift from E. Paluch (University of Cambridge,

UK). Walker cells and HL60 cells (RRID:CVCL_0002) were grown in T-25 suspension cell

culture flasks (Sarstedt, 83.3910.502) in RPMI 1640 media containing L-glutamine (Gibco,

11875101) supplemented with 10% heat-inactivated FCS and 1% penicillin-streptomycin

(Gibco, 10378016) at 37°C and 5% CO_2. The culture media for the HL60 cells additionally

contained 40 mM Hepes for buffering. Differentiation of HL60 cells was achieved by

incubating cells in propagation media plus 1.3% DMSO for 5 days. All working media was

passed through 0.2 μm Sartorius Minisart filters (VWR, 611-0691) prior to use. For

experiments, cells were transferred to media identical to their culture media except lacking

FCS. For myosin inhibition experiments, the imaging medium was additionally supplemented

with 30 μM of the ROCK inhibitor Y-27632 (Selleckchem, S6390), and an equivalent

volume of DMSO was added to the control condition. Cells were allowed to equilibrate in the

medium for 30 min before the start of the experiment.

Where appropriate, cells were labelled with Hoechst 33342 (Leica, H3570) at 1×10^{-5} mg/mL,

or BioTracker 490 Green Cytoplasmic Membrane Dye (Merck, SCT106) at 5 μL per 1 mL

cell suspension. In both cases, a concentrated cell solution was incubated with the marker for

30 min at 37°C before being washed out. Immunostaining against phospho-paxillin Tyr 118

(ThermoFisher, 44-722G) was performed by fixing in 4% paraformaldehyde for 10 min at

37°C followed by 0.1% Triton X-100 permeabilization for 15 min at RT, blocking in 2%

BSA/PBS for 1 hour at RT, 1:1000 primary antibody overnight at 4°C and a AlexaFluor goat

anti-rabbit secondary antibody (ThermoFisher, A-11008) at 1:500 for 4 hours at RT with PBS

washes in between antibody steps.

608

609 <u>Image processing, data analysis and statistics</u>

610 Images and videos were processed using Fiji. Cells were tracked using the Manual Tracking

611 plugin, and output data processed in the Chemotaxis and Migration Tool (Ibidi, Version 2.0).

612 In this manuscript, we have named Forward Migration Index as the Durotaxis Index, where

613 the axis of interest is along the stiffness gradient and where positive values indicate

614 straightness toward stiff substrate, and negative values indicate straightness toward soft

615 substrate.

616 To achieve high resolution imaging of cells across large regions, images were stitched for

617 analysis and presentation. Correction for uneven illumination was performed where

618 appropriate. Cells in contact with other cells were not included in the analysis, and tracks

619 were cut short where cell-cell contacts were made, to ensure only single cell analysis was

620 performed.

621 To quantify retrograde actomyosin flow independently from cell displacement, linear stack

622 alignment with SIFT was carried out in Fiji, and displacement was tracked manually in

623 kymographs, using the segmented line tool.

624 Normality in the spread of data for each experiment was tested using the Kolmogorov-

625 Smirnov, d'Agostino-Pearson, and Shapiro-Wilk tests in Prism9 (GraphPad9). Significances

626 for datasets displaying normal distributions were calculated in Prism9 with paired or unpaired

627 two-tailed Student's t-tests or Mann-Whitney U tests where appropriate. No predetermination

628 of sample sizes were done. Cells were allocated into experimental groups randomly. Authors

629 were not blinded because cells were selected prior to analysis. Criteria for selection was

630 survival and not interacting with other cells. All experiments were replicated three times

631 (biological replicates) unless otherwise indicated.

632

633 <u>Nanoindentation</u>

634 Stiffness measurements were performed using nanoindentation (Chiaro, Optics11Life, Piuma

635 V2 v3.4.3) as previously described[3]. Cantilevers were customized by Optics11 Life. Probes

636 had a spherical glass tip with a radius of ~ 10 μm mounted onto an individually calibrated

637 cantilever with a spring constant of ~ 0.25 N m^{-1}. Deformation of the cantilever after contact

638 with the sample was measured by tracking the phase-shift in light, reflected from the back of

639 the cantilever. Samples were indented to a depth of 0.5 μm with a velocity of 2.5 μm s^{-1}. The

640 tip was held at this indentation depth for 1 s and then retracted over 1 s. The Young's moduli

641 were calculated automatically by the software by fitting the force versus indentation curve to

642 the linear Hertzian contact equation model[35]. The effective Young's modulus (E), referred to

643 in this manuscript as stiffness, is derived from the fit of the loading force-displacement curve

644 ($F(h)$), the indenter tip radius (R), and the indentation depth (h), according to the following

645 formula, for which a Poisson's ratio (v) of 0.5 was assumed, and was calculated automatically

646 by the software (Chiaro, Optics11Life, Piuma V2 v3.4.3).

647
$$F = \frac{4}{3}K\sqrt{r}\delta^{\frac{3}{2}} = \frac{4}{3}\frac{E}{1-v^2}\sqrt{r}\delta^{\frac{3}{2}}$$

648

649 <u>Atomic force microscopy</u>

650 10 μm polystyrene beads were glued onto tipless MLCT B cantilevers (nominal spring

651 constant 0.02 N/m) and friction measurements were performed on the Nanowizard 4 AFM

652 system (Bruker Nano GmbH, JPK BioAFM) using Contact Mode. Lateral force was recorded

653 by sweeping the cantilever over a line of 10 μm length at a speed of 2.5 μm/s. We measured

654 the force at 5 kHz over a time frame of approximately 60 seconds to record several

655 oscillations. For each gel forces of 0.25, 0.5, 0.75, 1, 1.25, 1.5 and 1.75 nN was applied and

656 repeated at each force 5 times.

657

658   Micropatterning

659   PDMS or glass was plasma treated (Diener electronic) for 2 min and immediately coated with

660   100 µg/ml PLL(20)-g[3.5]-PEG(2) (Susos) or PLL(20)-g[3.5]-PEG(2)/FITC (Susos),

661   dissolved in PBS, for 30 min at room temperature. Surfaces were washed with 100 mM

662   Hepes pH 8-8.5 for 1h at room temperature and then incubated with 100 mg/ml mPEG-SVA

663   (Laysan Bio, MPEG-SVA-5000). Surfaces were washed in 1x PBS, followed by water, and

664   then air dried. The photoactivatable reagent, PLPP gel (Alvéole) was added at a ratio of 3:17

665   with 70% ethanol, at 1 µl PLPP gel/cm^2, and allowed to dry completely whilst protected from

666   light.

667   PRIMO (Alvéole) was calibrated with a 20x objective on a Nikon Ti inverted microscope

668   using Leonardo software (Alvéole). A greyscale pattern was used as shown in Extended Data

669   Fig. 8d. A dose of 30 mJ/mm^2 was used and laser power adjusted such that the patterning

670   time for each element was 4 s.

671   After patterning, the surface was washed several times with water and re-hydrated with PBS

672   for 5 min. The sample was then incubated with 50 µg/ml AlexaFluor647-conjugated BSA

673   (Thermo Fisher, A34785) overnight at 4°C prior to washing with PBS. Subsequent stages of

674   PDMS bonding to glass and imaging were performed as described in the Methods sections,

675   Soft lithography, and Imaging.

676

677   Photolithography

678   3-inch silicon wafers (Silicon wafer test grade, N(Phos), WAFER-SILI-0580W25 from PI-

679   KEM Ltd.) were plasma cleaned for 10 min at 100% power in a plasma cleaner (Henniker

680   Plasma HPT 100), and then baked on a hot plate at 200°C for 20 min to remove moisture.

681   After 10 s of cooling, SU-8 2005 (Kayaku Advanced Materials, purchased from A-Gas

682   Electronics Materials) was spin coated on the wafer at 500 rpm with an acceleration of 100

683   rpm s^{-1} for 30 s. After 2 min rest, the wafer was soft baked at 65°C for 1 min, followed by

684   95°C for 2 min, and then allowed to cool for 10 s. Writing was performed on a MicroWriter

685   ML3 using a 20x objective. Post-exposure bakes of the wafer were then performed at 65°C

686   for 1 min, 95°C for 2 min and then 65°C for 1 min. After 10 s cooling, the wafer was

687   developed in PGMEA (Sigma-Aldrich 484431-1L) for 1 min with manual agitation, before

688   rinsing in IPA for 10 s, dried with compressed N$_2$ and hard baked for 20 min at 200°C.

689   Dimensions of the wafer were analysed on an optical profiler (Sensofar S Neox).

690

691   <u>Soft lithography</u>

692   PDMS was made using reagents from a SYLGARD 184 Elastomer Kit (VWR, 634165S).

693   Base elastomer was thoroughly mixed with curing agent at a ratio of a ratio of 10:1, before

694   degassing in a vacuum desiccator (Scienceware, 999320237) with a KNF Laboport N96

695   diaphragm vacuum pump (Merck, Z675091-1EA). A Si wafer with positive features was

696   placed in a disposable aluminium dish (VWR, 611-1377), covered in PDMS, and baked for

697   10 min at 110°C. The PDMS was separated from the wafer and trimmed using a blade.

698

699   <u>Agarose microchannels</u>

700   PDMS was prepared as above, and spin coated onto a Si wafer with negative features using a

701   spin coater (Spin150) at conditions of 400 rpm for 30 s. The wafer was then baked at 110°C

702   for 10 min. The thin PDMS was peeled off from the wafer and cut into smaller pieces using a

703   razor blade, where each individual piece contained between one and four patterned designs.

704   To fabricate agarose microchannels, an individual PDMS piece was placed on a glass slide

705   with an edge aligned with the edge of the slide. A vacuum, and subsequently finger pressure,

706   was used to push trapped air bubbles out from underneath the PDMS. A ~1 mm thick piece of

707   PDMS was cut to generate a U-shape and placed around the PDMS pattern on the slide. A

708   coverslip was placed on top of the U-shape PDMS and neodymium magnets above the

709   coverslip and below the slide were used to secure the sandwich in place.

710   UltraPure low melting point agarose (ThermoFisher, 16520050) – in this manuscript referred

711   to as 'agarose' – was dissolved in RPMI media at the appropriate concentration, depending

712   on the experiment. The solution was maintained at 70°C while penicillin-streptomycin

713   (Gibco, 10378016) was added to a final concentration of 1%. To fabricate gels of uniform

714   stiffness, the agarose solution was pipetted into the sandwich until full. To fabricate gels of

715   graded stiffness, higher concentration agarose solution (4%) was pipetted into the sandwich

716   mid-way, followed by lower concentration agarose solution (1%) until full. The gradient was

717   modulated by modifying the diffusion rate, which could be controlled by incubating in an

718   oven at different temperatures, angles and by modifying the input solutions. To solidify the

719   agarose gels, the sandwich was transferred to a 4°C fridge. Afterwards, the sandwich was

720   disassembled and the solidified agarose slowly slid away from the underlying PDMS mould,

721   and reversed in orientation such that the structured agarose was face up. The surface was then

722   dried with a nitrogen gun and trimmed to size with a razorblade. The stiffness of agarose gels

723   was measured using a Chiaro nanointender (Methods, nanoindentation).

724   Holes were punched using a Harris uni-core 3 mm biopsy puncher (VWR, 89022-356),

725   followed by air drying with a nitrogen gun. A glass coverslip was then plasma cleaned and

726   bonded to the agarose microchannel chip, with the channels facing the coverslip. RPMI

727   media was pipetted into the holes and the unit placed in a humid chamber at 37°C and 5%

728   CO_2 for 30 min. The wells were then emptied using a p200 pipette and replaced with

729   concentrated cell solution. A 0.5 g weighted glass slide was placed on top of the structure,

730   and the unit placed in the stage of an inverted microscope.

731   Where appropriate, agarose surfaces were covalently bound to protein by using the CNBr-

732   method that has been reported previously[27,28]. After drying, agarose microchannels were

733   activated with cyanogen bromide: 50 mg/ml in water was mixed in an equal ratio with 0.5 M

734   Na_2CO_3 in NaOH buffer, pH 11, which contained the protein (fibronectin or PLL-g-PEG).

735   After 30 min, the surface was washed with water and then with the coupling buffer: 0.1 M

736   sodium borate buffer, pH 8.5 for 4 h.

737

738   Measuring the myosin intensity profile

739   Fluorescent live cell imaging was performed on a ZEISS Elyra 7 microscope equipped with a

740   40×, NA = 1.2 water-immersion objective and operating in laser WF mode. Time series of

741   single plane images along the cell-agarose interface were acquired in intervals of 10s. To

742   prevent GFP quenching, RPMI medium without phenol red (Thermo Fisher, 11835030) was

743   used in all experiments. Images were exported as TIF series for further analysis.

744   The experimental snapshots showed an intense myosin-GFP signal across the entire cell area

745   except for the nuclear region. We cropped individual snapshots by hand using Fiji to exclude

746   the background and nuclear region. We averaged the pixel intensities along the axis

747   perpendicular to the direction of motion to obtain a one-dimensional intensity profile $I(x)$

748   along the cell.

749

750   Numerical solution of the active gel model for amoeboid migration

751   To reduce the number of free parameters, we simplified the model. Firstly, we assumed that

752   the friction coefficient was constant. The equations in the model can be made independent of

753   the equilibrium volume fraction ϕ_0. This can be seen by rescaling the gel volume fraction

754   $\phi \rightarrow \phi_0\phi$, the pressure coefficient $\alpha \rightarrow \alpha/\phi_0^2$ and the drag coefficient $\xi_f \rightarrow \xi_f\phi_0$. We

755   therefore set $\phi_0 = 1$ without loss of generality. Finally, we made Eqs. S13-16 in the

756   Supplementary Note dimensionless as in Reference[24]. In dimensionless form, the model

757   contains 4 dimensionless parameters: the active stress coefficient $\bar{\zeta} = \zeta L^2/\gamma$, the

758   depolymerization rate $\bar{k}_d = k_d \xi L^4 / \gamma$, the pressure coefficient $\bar{\alpha} = \alpha L^2 / \gamma$, and the drag

759   coefficient $\bar{\bar{\xi}}_f = \xi_f / (\xi L)$.

760   We solved the dimensionless equations using the Method of Lines[36-38] to predict the time

761   variation of the steady-state gel volume fraction profile $\phi_{ss}(x, t)$ and the cell velocity $V(t)$

762   for migrating cells. We used centered finite differences to approximate the spatial derivatives.

763   Fictitious points were added outside the domain to define the spatial derivatives at the

764   boundaries. We used an explicit Euler step for the equations involving a time derivative and

765   we solved the remaining equations algebraically. We used 25-35 discretization points and a

766   time step of $\Delta t = 10^{-7}$. As initial conditions, we took the homogeneous state $\phi(x) = \phi_0$ plus

767   a small Gaussian-noise perturbation to each variable. The algorithm converges to provide a

768   steady-state gel volume fraction $\phi_{ss}(x)$ and the corresponding cell velocity V_{ss}.

769

770   <u>Fitting the model to the myosin intensity profiles</u>

771   We take the myosin intensity profile $I(x)$ from the experimental images as a proxy for the

772   concentration of the actomyosin cortex, given by its steady-state volume fraction $\phi_{ss}(x)$ in

773   the active gel model. However, we first had to select the region of the myosin intensity

774   profile that can be captured by the active gel model, given its assumptions. The model

775   captures cortical flow from low to high cortex concentrations and it assumes that the

776   concentration gradient vanishes at the rear and front of the cell. In contrast, experimental

777   myosin intensity profiles typically show extended intensity plateaus at each end of the cell,

778   which are connected by an intermediate intensity decay. To match the boundary conditions of

779   the model, we cropped the myosin intensity profiles to include only the intermediate decay

780   region and a small connected region of each plateau. In some cases, the myosin intensity at

781   the start of the plateau is obscured by the nucleus, so we roughly inferred where to crop the

782   profile by extrapolation. Also, cells 1 and 2 in Extended Data Fig. 6 have pronounced

783 uropods, which are myosin-rich tail structures that manifest as a second peak in the myosin

784 intensity profile at the rear side. We did not include the region of the uropod in the

785 comparison to the model. We indicate which region of each myosin intensity profile is

786 selected by means of vertical blue lines in Extended Data Figs. 6-7 (left-hand panels for each

787 cell).

788 We also had to scale the dimensions of the gel volume fraction $\phi(x)$ so that it could be

789 directly compared to the myosin intensity profile $I(x)$ in the selected region. The coordinate

790 along the cell was scaled linearly as $x \rightarrow xL$ to match the length L of the selected region.

791 Respectively, to fit it to the myosin intensity profile $I(x)$, we scaled the gel volume fraction

792 as $I(x) = I_0 \phi_{ss}(x)$, where I_0 is an additional free parameter in the fit.

793 Before performing the fits, we reduced the number of free parameters in the model. Firstly,

794 we fixed some of them: $\bar{\zeta} = 14$, $\bar{k}_d = 1$, and $\bar{\bar{\xi}}_f = 0.46$. These parameter values ensure that

795 the homogeneous state is only unstable to perturbations with a wavelength given by the cell

796 length. As a result, in this parameter regime, the model has steady-state gel volume fraction

797 solutions $\phi_{ss}(x)$ that decrease monotonically from the rear to the front of the cell. In addition,

798 each solution has an average value of gel volume fraction that is close to the equilibrium gel

799 volume fraction $\phi_0 = 1$. Therefore, for each snapshot, we calculated I_0 by measuring the

800 average myosin intensity in the selected region. In some cases, there was missing intensity

801 data in part of the selected region, due to the nucleus obscuring the myosin signal. Therefore,

802 we removed the intensity data at the opposite side of the selected region in calculating I_0,

803 which would otherwise skew the result.

804 By varying $\bar{\alpha}$, we performed a least-squares fit of the scaled steady-state volume fraction to

805 the myosin intensity profile in the selected region for each cell at a single time frame. We

806 show the fits in Extended Data Figs. 6-7 (right hand panels for each cell), and the

807 corresponding parameter values in Table I.

Author contributions

A.S. and K.W. conceived the project, performed the experiments, and analysed the experimental data. R.A. and P.H. developed the physical model and derived the explanation of frictiotaxis. P.H. solved the model numerically and fitted it to the experimental data. N.S. contributed to conceptualisation of the model and performed AFM with R.T. with assistance from G.C. G.C. provided conceptual and technical advice, especially with AFM and tissue culture. A.S and C.D. generated the silicon wafers in A.I.'s laboratory. A.S., K.W., R.M. and R.A. wrote and edited the manuscript. All authors commented on the manuscript.

Competing interests

The authors declare that they have no competing interests.

833

Data and materials availability

835   All data are available in the main text or the supplementary materials.